

Isotopic Transparency in Central Xe+Sn Collisions at 100 MeV/nucleon

A. Le Fèvre^{a,*}, A. Chbihi^b, Q. Fable^c, T. Génard^b, J. Lukasik^d,
W. Trautmann^a, K. Turzó^a, R. Bougault^e, S. Hudan^f, O. Lopez^e,
W.F.J. Müller^a, C. Schwarz^a, C. Sfiendi^g, G. Verde^{c,h}, M. Vigilanteⁱ,
B. Zwiegliński^j

^aGSI Helmholtzzentrum für Schwerionenforschung GmbH, D-64291 Darmstadt, Germany

^bGANIL, CEA et IN2P3-CNRS, F-14076 Caen, France

^cLaboratoire des 2 Infinis - Toulouse (L2IT-IN2P3), Université de Toulouse, CNRS, UPS, F-31062 Toulouse Cedex 9, France

^dH. Niewodniczański Institute of Nuclear Physics, PL-31342 Kraków, Poland

^eUniversité de Caen Normandie, ENSICAEN, CNRS/IN2P3, LPC Caen UMR6534, F-14000 Caen, France

^fDepartment of Chemistry and Center for Exploration of Energy and Matter, Indiana University, Bloomington, Indiana 47408, USA

^gInstitute of Nuclear Physics, Johannes Gutenberg University, D-55099 Mainz, Germany

^hINFN Catania, Italy

ⁱDipartimento di Scienze Fisiche e Sezione INFN, Univ. Federico II, I-80126 Napoli, Italy

^jNational Centre for Nuclear Research, PL-02093 Warsaw, Poland

Abstract

A new method, based on comparing isotopic yield ratios measured at forward and sideward polar angles and on cross-bombarding heavy nuclei with different neutron-to-proton ratios, is used to quantify the stopping power of nuclear matter in heavy-ion collisions. For central collisions of isotopically separated $^{124,129}\text{Xe}+^{112,124}\text{Sn}$ at 100 MeV/nucleon bombarding energy, measured with the 4π multidetector INDRA at GSI, a moderate transparency is deduced for hydrogen isotopes, whereas for heavier fragmentation products with atomic number $Z \geq 3$ a high transparency exceeding 50% is observed. An anomalously large transparency is found for alpha particles, and possible explanations are presented.

Keywords: NUCLEAR REACTIONS, $^{112,124}\text{Sn}(^{124,129}\text{Xe}, X)$, $E = 100$ MeV/nucleon, multifragmentation, breakup state, isotopic effects, transparency, nuclear matter stopping power

Stopping is an important property identifying the nature of heavy-ion collisions [1]. Its variation with the incident energy characterizes the evolution of the collision dynamics. At incident energies above the Coulomb barrier, the

*corresponding author: A.LeFevre@gsi.de

dependence of compound nucleus formation and dissipative binary collisions on impact parameter has been described within the concepts of critical angular momentum and surface friction [2, 3, 4, 5, 6]. Above the Fermi-energy domain, nucleon-nucleon collisions govern the dynamics, and stopping in central collisions is of particular interest because dense matter may be formed in the collision zone, offering the possibility of studying the equation of state of nuclear matter beyond its saturation properties (Refs. [7, 8, 9, 10] and references therein).

An observable conveniently used to measure the degree of relaxation of the initial momentum is the isotropy ratio

$$R_p = \frac{\langle p_x^2 \rangle + \langle p_y^2 \rangle}{2 \langle p_z^2 \rangle} \quad (1)$$

describing the strengths of the variances of transverse momenta p_x and p_y relative to that of the longitudinal momenta p_z of reaction products in the center-of-mass (c.m.) frame [11, 12, 13]. The ratio $R_p = 1$ indicates complete stopping with the production of an isotropic momentum distribution, a situation hardly reached at intermediate bombarding energies. The excitation function for stopping in central $^{197}\text{Au}+^{197}\text{Au}$ collisions over the incident energy range from 15 MeV/nucleon up to 1.5 GeV/nucleon exhibits a rise from $R_p \approx 0.5$ near 40 MeV/nucleon to a maximum of 0.9 at 600 MeV/nucleon and a wide plateau with values exceeding 0.8 at energies between 200 MeV/nucleon and 1 GeV/nucleon (FOPI and INDRA data, Andronic et al. [12]). The energy range up to 100 MeV/nucleon was investigated in detail by Lehaut et al. [14] who used data for several mass-symmetric reactions from Ar+KCl to $^{197}\text{Au}+^{197}\text{Au}$ which had been studied with the INDRA multidetector [15]. A general trend of isotropy ratios near 0.6 exhibiting a weak rise with incident energy is reported for the selected central event classes.

The formation of composite systems with longitudinally elongated momentum distributions is thus found to be a general feature of central heavy-ion collisions at intermediate energies. It can be the result of a transparency, i.e. of an incomplete stopping of the incoming projectile by the target as, e.g., observed by the FOPI collaboration for Zr+Ru central collisions at 400 MeV/nucleon [16]. This phenomenon is manifested by an incomplete relaxation of momenta and by angular anisotropies of fragment yields, as reported by the INDRA collaboration for $^{197}\text{Au}+^{197}\text{Au}$ and $^{129}\text{Xe}+\text{natSn}$ central collisions at energies between 40 and 150 MeV/nucleon [13, 17, 18, 19, 20].

Several approaches were used to interpret the anisotropies observed in fragment productions. The study of central $^{129}\text{Xe}+\text{natSn}$ and $^{197}\text{Au}+^{197}\text{Au}$ collisions at bombarding energies between 50 and 100 MeV/nucleon demonstrated that an accurate statistical description of the measured anisotropies in fragment yields and kinetic energies is obtained if a prolate source deformation and a superimposed collective motion are included [17]. The element yields were found to extend to larger atomic numbers Z at forward and backward emission angles than at sideward angles. In the Metropolis Multifragmentation Monte Carlo

(MMMC) model used in that work, an important role is played by the Coulomb interaction which favors large spatial separations between heavy fragments in order to minimize the Coulomb energy [17]. Heavy fragments are preferentially placed in the tips of a prolate source. Through the Coulomb repulsion and the superimposed radial flow, these spatial correlations induce correlations in momentum space which lead to the observed maxima in the yields and kinetic energies of the heaviest fragments at forward and backward directions.

This scenario was confirmed in a study using correlation functions constructed from directional projections of the relative velocities of fragments which was applied to central $^{129}\text{Xe}+^{\text{nat}}\text{Sn}$ collisions at 50 MeV/nucleon [18]. It showed that the predicted correlation functions obtained from MMMC calculations depend strongly on the chosen source geometry at breakup. Assuming a prolate deformation of the breakup volume in coordinate space, aligned along the beam direction, permitted a satisfactory description of the experimental data.

With a quantum molecular dynamics approach, the anisotropies observed in central $^{197}\text{Au}+^{197}\text{Au}$ collisions between 60 and 150 MeV/nucleon bombarding energy were successfully reproduced [13]. It was shown that the fragment compositions close to midrapidity can be described by statistical laws whereas they are dominated by the dynamics at large and small rapidities. A sizeable fraction of the initial momentum is not relaxed: the majority of fragments represent surviving initial-final state correlations and are not substantially decelerated in longitudinal direction. In this dynamical approach, the stopping power of nuclear matter is found to be strong for hydrogen isotopes but decreasing with atomic number Z and very small for heavier fragments.

Table 1: For each system, from left to right: N/Z value of the combined system, thresholds of M_c and of $E_{\perp 12}$ corresponding to a reduced impact parameter $b/b_{\text{max}} = 0.1$ (see text). The enrichment of the Sn targets is taken into account.

System	N/Z	M_c	$E_{\perp 12}$ (MeV)
$^{124}\text{Xe}+^{112}\text{Sn}$	1.270	50	1463
$^{129}\text{Xe}+^{112}\text{Sn}$	1.318	50	1455
$^{124}\text{Xe}+^{124}\text{Sn}$	1.385	50	1465
$^{129}\text{Xe}+^{124}\text{Sn}$	1.433	49	1451

The aim of the present work is to quantify the stopping power of nuclear matter in central collisions, on a pure experimental basis, by using the isotopic composition of the emitted particles and fragments as observables capable of identifying the primary sources in which they are formed [21, 22, 23]. The degree of mixing of nucleons of the target and of the projectile that has occurred in the course of the collision and the observed chemical equilibration will complement the information provided by the momentum observables. Measurements

at sideward angles, at which full mixing follows from the approximate mass symmetry of the four collision systems, are used as a base line for the interpretation. A statistical description is found useful for this purpose but we do not intend to explain in this work the mechanism by which clusters are formed.

We report data for Xe+Sn collisions at 100 MeV/nucleon incident energy, obtained at the GSI laboratory with the INDRA multidetector [15]. By cross-bombarding enriched targets of ^{112}Sn (98.9%) and ^{124}Sn (99.9%) with $^{124,129}\text{Xe}$ projectiles, neutron-over-proton ratios N/Z of the combined system ranging from 1.27 to 1.43 were covered (Table 1). Details of the setup and data calibration for this experiment are found in Ref. [17].

Central collisions were selected either according to the total multiplicity of charged particles M_c or with the total transverse kinetic energy $E_{\perp 12}$ of light charged particles with $Z = 1, 2$. In both cases, only 1% of the recorded reaction cross sections were accepted, corresponding to a reduced impact parameter $b/b_{\text{max}} \leq 0.1$ in sharp-cut-off approximation and assuming a monotonic relation of M_c or $E_{\perp 12}$ with the impact parameter. The acceptance thresholds were found to be rather similar for the four studied reactions with thresholds $M_c \approx 50$ and $E_{\perp 12} \approx 1460$ MeV (Table 1). It is obvious that these high thresholds cut into the tails of the M_c and $E_{\perp 12}$ distributions. As demonstrated in [13], these tails may be partly caused by the fluctuation widths of M_c and $E_{\perp 12}$ in central collisions rather than by a significant variation of the impact parameter up to the highest values of these variables.

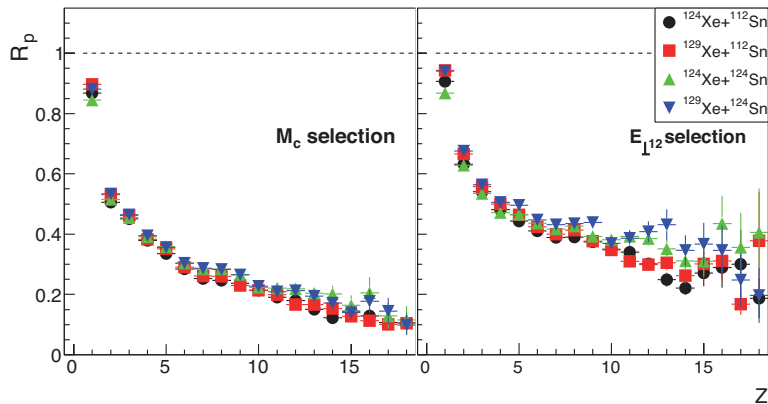


Figure 1: Isotropy ratio R_p as a function of the fragment atomic number Z for the four combinations of $^{124,129}\text{Xe}+^{112,124}\text{Sn}$ reactions at 100 MeV/nucleon incident energy in central collisions selected according to M_c (left panel) and $E_{\perp 12}$ (right panel).

The isotropy ratio R_p defined in Eq. (1) is displayed in Fig. 1 as a function of the fragment Z for the central event classes of the four systems, selected according to M_c or $E_{\perp 12}$. In the latter case, in order to avoid autocorrelations

between the R_p values for $Z = 1, 2$ and $E_{\perp 12}$, the centrality criterion $E_{\perp 12}$ was calculated without the particle of interest. A $Z = 1$ or $Z = 2$ particle whose exclusion from $E_{\perp 12}$ makes the event no longer “central” is not taken into account in the calculation of R_p for this particular Z .

We observe the same trend for both selections and all systems. The isotropy ratio R_p is close to 1 for hydrogen isotopes, indicating full relaxation of the initial momenta, but decreases rapidly with the fragment atomic number. The momenta of the larger fragments are predominantly oriented in longitudinal directions. The ratio R_p is found to be significantly higher with $E_{\perp 12}$ than with M_c centrality selections. This is possible because the M_c and $E_{\perp 12}$ selected event groups are only partly overlapping as documented for similar reactions in Fig. 3 of Ref. [17]. The transfer of transverse momentum to light particles with $Z = 1, 2$ and to fragments with intermediate mass is apparently correlated. Choosing reactions with highest $E_{\perp 12}$ thus favors the cases for which the largest stopping has occurred. In addition, there is no visible influence of the initial isotopic compositions on R_p in the case of the M_c selection whereas, with the $E_{\perp 12}$ selection, the ratio R_p increases with the N/Z of the collision system for the larger Z values (Fig 1). The mode of selecting central events has a measurable influence on the resulting momentum configuration.

For the elements with atomic number $Z \leq 4$ considered in the following, the INDRA multidetector offers excellent isotopic resolution [15]. In the nine forward rings (at polar angles $\theta_{\text{lab}} \leq 45^\circ$), the mass identification for light elements with sufficiently high velocity is possible using the maps of the fast versus the slow components of the light detected in the detectors made of cesium-iodide scintillating crystals doped with thallium (CsI(Tl)). Alternatively, the maps of the signals recorded by the 300- μm silicon detectors versus the total light in the CsI(Tl) detectors may be used. At angles beyond 45° , at which INDRA is not equipped with silicon detectors, the fast versus slow maps of the CsI(Tl) signals are used for mass identification.

The measured two-dimensional invariant distributions in the transverse versus longitudinal rapidity space of deuterons, ^4He , and ^7Li isotopes are displayed in Fig. 2. The yields of the three isotopes are well covered by the acceptance of the INDRA multidetector within both, the forward and sideward angular cuts in the center-of-mass system chosen for the analysis: polar angles $\theta_{\text{cm}} \leq 34^\circ$ and $80^\circ \leq \theta_{\text{cm}} \leq 100^\circ$, respectively. As shown in Fig. 2, center-of-mass emissions to sideward angles are spread over most of the rings in the forward hemisphere of the INDRA detector and identified on the basis of the measured kinetic energies. The c.m. yields in forward direction are spread over fewer INDRA rings and selected with a ring dependent lower threshold of the kinetic energies. The angular cuts are clearly approximate within these limits but essentially identical for the four reactions.

The coverage is similar for the remaining isotopes up to $^{7,10}\text{Be}$. The decreasing degree of stopping with increasing fragment mass is as well evident in Fig. 2. In fact, the sideward emissions of, e.g., ^7Li fragments are no longer representing the central part of the distribution but originate from the tail connecting the forward and backward moving groups.

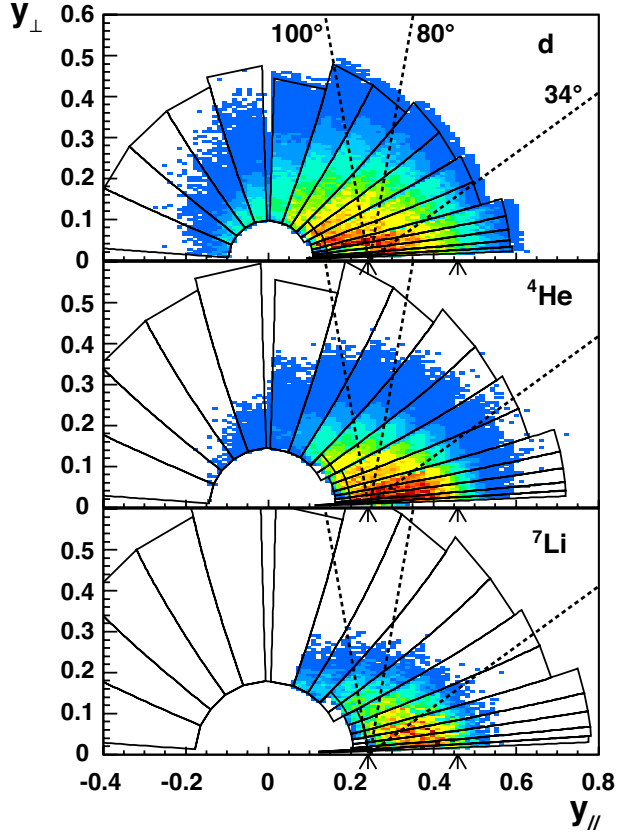


Figure 2: Two-dimensional invariant distributions in the transverse versus longitudinal rapidity space of deuterons, ${}^4\text{He}$, and ${}^7\text{Li}$ isotopes (top to bottom) for Xe+Sn central collisions at 100 MeV/nucleon incident energy. Dashed lines represent the forward and sideward acceptance cuts in the center-of-mass frame ($\theta_{\text{cm}} \leq 34^\circ$ and $80^\circ \leq \theta_{\text{cm}} \leq 100^\circ$, respectively). Full lines depict the geometrical acceptance of the 17 rings of the INDRA multidetector, including high and low energy thresholds. The arrows below the x-axes at $y_{\parallel} = 0.46$ and 0.23 mark the longitudinal rapidities of the projectiles and of the center-of-mass system assuming mass symmetry, respectively.

We present in Fig. 3, left panel, the yield ratios of several light isotopes emitted at sideward angles in the center-of-mass ($80^\circ \leq \theta_{\text{cm}} \leq 100^\circ$) as a function of the total N/Z of the system for central collisions selected with M_c (cf. Table 1). Their exponential dependence on N/Z , observed for all cases, is remarkable. It reflects the full mixing of target and projectile matter expected at mid-rapidity [24, 25].

The logarithmic slope parameters α of exponential fits are found to be proportional to the difference ΔN of the neutron numbers of the two isotopes

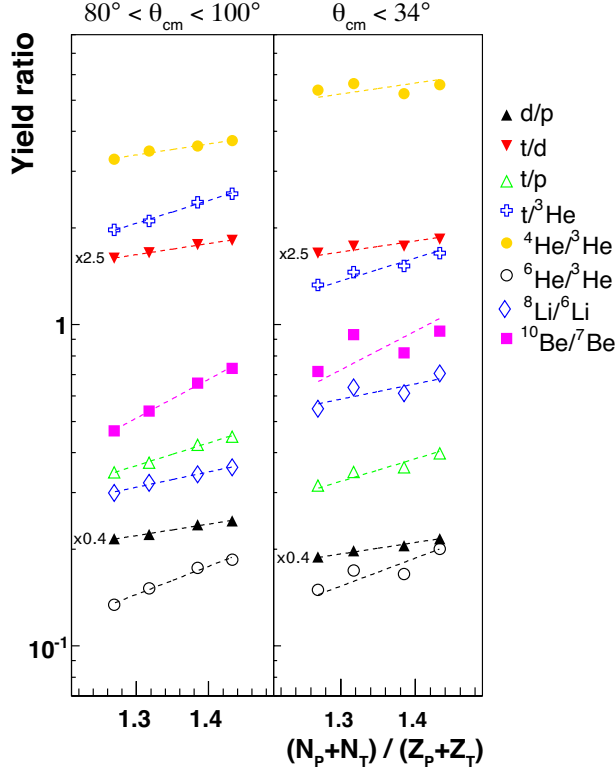


Figure 3: Isotope yield ratios as functions of the total N/Z of the system in central collisions, selected according to M_c , of $^{124,129}\text{Xe}+^{112,124}\text{Sn}$ at 100 MeV/nucleon, for sideward angles (left panel, $80^\circ \leq \theta_{\text{cm}} \leq 100^\circ$) and forward angles (right panel, $\theta_{\text{cm}} \leq 34^\circ$). To avoid overlaps of data symbols, the indicated factors were applied to the measured d/p and t/d ratios. Statistical errors range from below 1% for light particles up to ≈ 3 or 4% for the Li and Be ratios and are smaller than the size of the symbols. The lines represent exponential fits to the ratios. In the right panel, to facilitate comparisons, fits are constrained to reproduce the slopes found in the left panel.

forming a pair (Fig. 4), suggesting a statistical emission pattern in the grand-canonical description [26]. Qualitatively the same results are obtained when $E_{\perp 12}$ is used to select central events, with the exception that the measured ratios are, on average, 4% larger with $E_{\perp 12}$ than with M_c as selection criterion. The average value of the absolute differences between the ratios obtained with the two selections is $\approx 6\%$. This is larger than the statistical errors and may thus serve as an estimate of the overall experimental uncertainties.

The application of grand-canonical sampling permits a global understanding of the measured isotope ratios. In its simplest form, the yield ratios of isotopes differing by ΔN neutrons can be expressed as

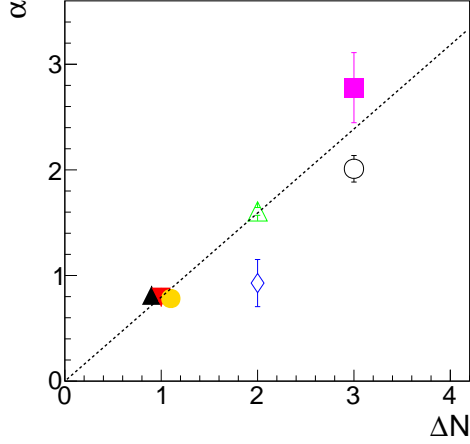


Figure 4: Slopes α of exponential fits extracted from Fig. 3, left panel (sideward emissions, M_c selection), as a function of the difference ΔN in neutron number of the isotope pair. The $t/{}^3\text{He}$ isobar ratio is not included. The displayed errors are those returned by the fit routine. The dotted line represents the weighted mean of the rise of α with ΔN . The symbols are chosen as in Fig. 3. For better visibility, the symbols related to the t/d and ${}^4\text{He}/{}^3\text{He}$ ratios are slightly shifted horizontally.

$$\frac{Y(A_2, Z)}{Y(A_1, Z)} = \left(\frac{A_2}{A_1}\right)^{3/2} \frac{\omega(A_2, Z)}{\omega(A_1, Z)} \exp\left(\frac{\Delta N \times \mu_n + \Delta B}{T}\right) \quad (2)$$

with A_1 and $A_2 = A_1 + \Delta N$ representing the mass numbers of the two isotopes, $\omega(A_i, Z)$ their internal partition functions, and $\Delta B = B_2 - B_1$ the difference of their binding energies [27, 28]. The chemical potentials μ_n of neutrons and μ_p of protons guarantee the conservation of the mean mass and charge of the disassembling system within a given volume and thus are functions of its N/Z ratio. The chemical potential μ_p of protons appears only in the $t/{}^3\text{He}$ isobar ratio involving nuclides with different Z . The assumption that the chemical potentials depend, to first order, linearly on N/Z immediately explains the experimental finding that, in the apparently equilibrated case at sideward angles, the logarithm of the ratio increases linearly with the N/Z ratios of the emitting sources.

The grand-canonical predictions shown in Table 2 were obtained in the following way. For the temperature T , the double-isotope temperature [28, 29, 30]

$$T_{\text{Hedt}} = 14.31 \text{ MeV} / \ln\left(1.59 \frac{Y_d/Y_t}{Y_{{}^3\text{He}}/Y_{{}^4\text{He}}}\right) \quad (3)$$

was chosen and determined from the experimental values at $N/Z = 1.35$ as given by the exponential fits of the four measured ratios (Fig. 3, left panel).

A value $T_{\text{Hedt}} = 6.82 \pm 0.28$ MeV was obtained and used to determine the chemical potential $\mu_n = -10.20 \pm 0.32$ MeV for neutrons from either one of the t/d or ${}^4\text{He}/{}^3\text{He}$ yield ratios (the errors are obtained using the 6% uncertainty of the yield ratios quoted above; see Ref. [30] for a discussion of systematic uncertainties of double-isotope temperatures). These values together with the t/ ${}^3\text{He}$ yield ratio determine also the chemical potential $\mu_p = -14.95 \pm 0.51$ MeV for protons [30]. The ground-state spin j was used for the internal partition functions $\omega = 2j + 1$ for light particles with $Z \leq 2$. For the heavier isotopes ${}^6,8\text{Li}$ and ${}^7,10\text{Be}$, all states up to the lowest particle threshold were included with a weight $\exp(-E_x/T_{\text{Hedt}})$ given by their excitation energies E_x . For ${}^{10}\text{Be}$, e.g., a total of six states including the ground state were considered. The same weights were applied to determine weighted averages for the binding energies of these four isotopes. Nevertheless, since secondary decays are not taken into account, the obtained results can only be approximate (cf. Ref. [26]). The very similar chemical potentials $\mu_n = -11.2$ MeV and $\mu_p = -16.0$ MeV for a temperature $T = 6$ MeV for sideways emissions in the same reaction were recently reported by Bonnet et al. [31].

Table 2: Predictions according to Eq. (2) for the indicated pairs of isotopes for the temperature $T = 6.82$ MeV and the chemical potential $\mu_n = -10.20$ MeV for neutrons in comparison with the experimental yield ratios (last column; M_c selection) as given by the exponential fits for $N/Z = 1.35$ (Fig. 3, left panel). The t/ ${}^3\text{He}$ isobar ratio is used to derive the chemical potential $\mu_p = -14.95$ MeV for protons. ΔB is given in MeV; ω_2/ω_1 denotes the ratio $\omega(A_2, Z)/\omega(A_1, Z)$ of the internal partition functions appearing in Eq. 2; see text for further details.

isotopes	$(A_2/A_1)^{3/2}$	ω_2/ω_1	ΔB	pred.	exp.
d/p	2.83	1.50	2.22	1.32	0.57
t/d	1.84	0.67	6.26	0.69	0.69
t/p	5.20	1.00	8.48	0.90	0.39
t/ ${}^3\text{He}$	1.00	1.00	0.76	2.24	2.24
${}^4\text{He}/{}^3\text{He}$	1.54	0.50	20.57	3.52	3.52
${}^6\text{He}/{}^3\text{He}$	2.83	0.50	21.55	0.38	0.16
${}^8\text{Li}/{}^6\text{Li}$	1.54	0.88	10.46	0.31	0.32
${}^{10}\text{Be}/{}^7\text{Be}$	1.71	0.98	24.72	0.71	0.59

The yield ratios measured for t/d, ${}^4\text{He}/{}^3\text{He}$, and t/ ${}^3\text{He}$ are reproduced exactly by construction, and others are well approximated (last two columns of Table 2). The d/p and t/p ratios are overpredicted by factors of ≈ 2.3 . There seem to be more than twice as many protons emitted as expected. The special role of protons has already been noticed in previous cases [24, 28] and was shown to be related to early out-of-equilibrium emissions in Ref. [24]. Calculations with dynamical models capable of describing the fragment production in

comparable reactions [13, 32, 33] could be useful for addressing this issue.

The ${}^6\text{He}/{}^3\text{He}$ yield ratio is also overpredicted by a similar factor. It is somewhat surprising because, for the binding energy and statistical weight, only the ground state of ${}^6\text{He}$ is taken into account. One may suspect that further interactions until kinetic freeze-out reduce the yields of ${}^6\text{He}$ which is known to have the extended spatial distribution of a halo nucleus [34], actually the only isotope of this kind included in this study. It is still remarkable that the latter three ratios obey the observed systematics of the slopes $\alpha = \Delta N \times (0.79 \pm 0.02)$ (Fig. 4) which, in the grand-canonical approximation, are given by $\alpha = \Delta N \times d\mu_n/d(N/Z)/T$, assuming that the temperature T is the same for the four reactions. Interestingly, the obtained α has less than half the values observed for lithium up to carbon isotope ratios in the mass-asymmetric reactions studied by Wada et al. [24] and Déak et al. [35], possibly indicating lower emission temperatures there. The expected exponential dependence on the binding-energy difference (cf. Eq. 2) has been observed for the yield ratios of the mirror nuclei $t/{}^3\text{He}$, ${}^7\text{Li}/{}^7\text{Be}$, and ${}^{11}\text{B}/{}^{11}\text{C}$ in Sn+Sn reactions by Xu et al. [36].

The obtained source properties T , μ_n , and μ_p compare well with values given by the more sophisticated statistical models QSM (Quantum Statistical Model [37]) and SMM (Statistical Multifragmentation Model [38]) for sources of low density. In these models, chemical potentials as derived here from the yield ratios of light fragments and temperatures around 6 MeV refer to excited sources with density near or below one third of the nuclear saturation density (cf. Figs. 4 and 6 in Ref. [39]). Freeze-out densities of this magnitude have been deduced from measured correlation functions [40, 41, 42] and are successfully used in statistical descriptions of multifragmentation data (see, e.g., Refs. [17, 23, 43, 44] and references given therein).

Summarizing this section, we may conclude that the grand-canonical approximation gives a sufficiently accurate description of the sideward emission rates, permitting a qualitative understanding of the observed yield ratios spread over two orders of magnitude. For improvements, models like the SMM explicitly treating secondary fragment decays may be appropriate.

Proceeding now from the chemically equilibrated sideward emissions to the yield ratios obtained at forward angles for the same centrality classes (Fig. 3, right panel), we find similar trends and somewhat different average values but also a significant difference. As a function of the total N/Z , a characteristic step pattern is observed which is common to all eight cases. To highlight the differences, the exponential fits shown in the right panel of Fig. 3 are constrained to reproduce the slopes found in the left panel. Compared to the sideward emissions, the variation of ratios measured in different reactions is larger if the projectile is exchanged and smaller if the target is exchanged, indicating an incomplete isospin equilibration between the projectile and target matter for the reaction products at forward angles.

These observations are used to derive an isotopic transparency τ for each of the eight pairs of nuclides according to the relation

$$\tau = \frac{\tau_P - \tau_T}{\tau_P + \tau_T} \quad (4)$$

in which τ_P and τ_T measure the relative proportions of projectile-like and target-like contributions, respectively, to the isotopic compositions that are observed at forward angles. The definition of these coefficients relies on the correlation of the measured yield ratios with the total N/Z of the colliding system and on the exponential dependence describing it as observed at sideward angles (Fig. 3, left panel). For example, τ_P is obtained as the logarithm of the ratio of the yield ratios from two reactions with different projectiles on the same target, normalized with the difference $\Delta(N/Z)_P = 0.093$ of the neutron-over-proton ratios of the two projectiles according to

$$\tau_P = \frac{\ln(R_1/R_2)}{\Delta(N/Z)_P}. \quad (5)$$

Here R_1 and R_2 denote the two forward yield ratios with R_1 being that for the case with the more neutron-rich projectile. This can be done with either one of the two targets, and we use the average value of the two possibilities. Similarly, τ_T is obtained from comparing pairs of reaction systems with different targets but the same projectile and with the difference $\Delta(N/Z)_T = 0.238$ of the two target nuclei as normalization. In the case of full isospin equilibration, as represented by the exponential fits at sideward angles, the numerators $\ln(R_1/R_2)$ are equal to $(\alpha\Delta(N_P + N_T))/(Z_P + Z_T)$ and thus $\tau_P = 0.52\alpha$, $\tau_T = 0.48\alpha$ and $\tau = 0.04$ for the present nearly mass-symmetric reaction systems. Note that α cancels in the expression for τ . A transparency of 100%, when the yield ratios do not depend on the target, causes $\tau_T = 0$ and thus $\tau = 1$. A bounce-back would lead to negative values of τ which, however, is neither expected nor observed. The finally obtained values are all positive (Fig. 5 and Table 3).

The isotopic transparencies derived with the two methods of choosing the central event group are statistically consistent even though, for light particles up to $A \leq 4$, a preference for slightly smaller values in the case of the $E_{\perp 12}$ selection may be present. However, independent of the chosen method, the same systematic trend is observed. The transparency is very moderate for hydrogen isotopes and $t/^3\text{He}$ ($\tau \approx 20 - 45\%$) whereas transparency values exceeding 50% are obtained for heavier products. These results were confirmed by a recent analysis of the same data, selecting central events up to 4% of the recorded cross section with a third method and using similar angular cuts [45].

One may argue that the incomplete overlap of projectile and target at finite impact parameters can mimic transparencies for geometric reasons. In fact, the actual distribution of impact parameters is expected to reach beyond the sharp-cutoff limit $b/b_{max} \leq 0.1$ corresponding to the selected most central 1% of the cross section. Following Ref. [12], it is more likely a typical impact parameter rather than a maximum value. Even though the incident energy 100 MeV/nucleon is far below the regime at which the participant-spectator model is seriously applicable, its predictions may still be useful for estimating the order of magnitude of possible spectator contributions at forward angles. According

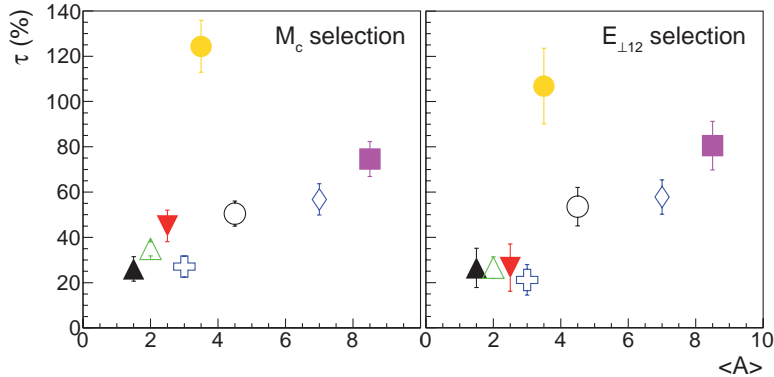


Figure 5: Transparency τ of forward emissions for the studied isotope pairs produced in central collisions of $^{124,129}\text{Xe}+^{112,124}\text{Sn}$ at 100 MeV/nucleon selected according to M_c (left panel) and $E_{\perp 12}$ (right panel). The symbols are chosen as in Figs. 3 and 4 and placed at the mean mass values of the isotope pairs. The numerical values are given in Table 3.

to the formulae presented by Gosset et al. [46], the spectator matter appearing at $b/b_{max} \approx 0.1$ in collisions of approximately equal size nuclei amounts to about 10% which is small with respect to the observed isotopic transparencies.

Table 3: Transparency τ (in percent) as derived from forward emissions ($\theta_{cm} \leq 34^\circ$) for the studied isotope pairs produced in central collisions of $^{124,129}\text{Xe}+^{112,124}\text{Sn}$ at 100 MeV/nucleon and selected according to M_c and $E_{\perp 12}$. Only statistical errors are given.

	d/p	t/d	t/p	t/ ^3He
$\tau(\%) M_c$ sel.	26 ± 5	45 ± 7	35 ± 3	27 ± 5
$\tau(\%) E_{\perp 12}$ sel.	25 ± 9	26 ± 10	27 ± 5	21 ± 7
	$^4\text{He}/^3\text{He}$	$^6\text{He}/^3\text{He}$	$^8\text{Li}/^6\text{Li}$	$^{10}\text{Be}/^7\text{Be}$
$\tau(\%) M_c$ sel.	124 ± 12	50 ± 6	56 ± 7	75 ± 8
$\tau(\%) E_{\perp 12}$ sel.	107 ± 17	53 ± 9	58 ± 8	80 ± 11

An anomalous transparency exceeding 100% is derived from the $^4\text{He}/^3\text{He}$ yield ratio for the selection with M_c and nearly as high for the selection with $E_{\perp 12}$. It is associated with a forward enhancement of the ^4He emissions contrasting those of ^3He and other light particles with $Z = 1, 2$. By using the values for t/ ^3He , the ratios of $^{3,4,6}\text{He}$ with respect to protons for $N/Z = 1.35$ can be determined from the experimental results listed in Table 2 and from the corresponding data for forward emission and the $E_{\perp 12}$ selections. The forward-

to-sidewards ratio of ${}^4\text{He}/\text{p}$ is 2.08 (1.52) for the case of $M_c(E_{\perp 112})$ selections and thus significantly larger than the average forward to sidewards ratios 1.13 ± 0.15 (1.03 ± 0.10) of the remaining four yield ratios of $Z = 1, 2$ particles with respect to protons (the quoted errors are rms values). As hydrogen isotopes exhibit a close to complete momentum relaxation (Fig. 1), it follows that essentially only the ${}^4\text{He}$ angular distribution is longitudinally extended. Because $\approx 80\%$ of the $Z = 2$ yields are ${}^4\text{He}$, this fact is also evident in Fig. 1.

The observed $\approx 100\%$ transparency, in addition, indicates that α particles observed at forward angles mostly originate from the projectile. Their forward enhancement is thus not unexpected because, similar to neutrons [47], they are more likely produced in secondary deexcitations of heavier products than p, d, t, or ${}^{3,6}\text{He}$ particles, thereby carrying part of the longitudinal momenta of the heavy nuclei emitting them. A second possible interpretation relates to the participant-spectator picture briefly evoked above. Alpha clustering of the non-interacting surface parts of low density in very central collisions may be another reason for the observed high ${}^4\text{He}/{}^3\text{He}$ transparency [48, 49]. In fact, if these parts of the projectile surfaces remain larger in collisions with the smaller ${}^{112}\text{Sn}$ target than in collisions with ${}^{124}\text{Sn}$, their clusterization may even explain the inverted target dependence, i.e. larger ${}^4\text{He}/{}^3\text{He}$ ratios with the neutron-poor ${}^{112}\text{Sn}$ target (Fig. 3, right panel). The inversion causes the anomalous transparency of more than 100% that is exclusively observed for ${}^4\text{He}/{}^3\text{He}$ (Fig. 5).

Finally, comparing the so obtained isotopic transparency with the isotropy ratio R_p (Fig. 1), we observe very consistent common trends. The average $R_p \approx 0.7$ for $Z = 1$ and 2 is associated with $\tau \approx 30\%$ (Table 3, upper part), both reflecting significant stopping and momentum equilibration for the light-particle emission. For the Be isotopes, the largest fragments considered here, the high transparency exceeding 70% confirms the interpretation that the moderate isotropy ratio $R_p \approx 0.4$ is caused by the incomplete stopping of significant amounts of projectile material, even in the selected very central collisions. The present isotopic study thus supports and complements the conclusions reached in the dynamical [13, 32] and statistical [17] interpretations of fragmentation at the present energy which falls into the transition regime toward the participant-spectator scenario at relativistic energies.

In summary, the INDRA multidetector with a solid-angle coverage of nearly 4π was used in experiments conducted with xenon beams of 100 MeV/nucleon from the SIS18 synchrotron at the GSI laboratory to study isospin equilibration in central collisions in the approximately mass symmetric ${}^{124,129}\text{Xe}+{}^{112,124}\text{Sn}$ reactions. The N/Z interval covered with the four projectile-target combinations extended from 1.27 to 1.43, large enough to observe significant variations of the measured yield ratios of isotopically resolved reaction products with mass numbers $A \leq 10$. Sideward emissions at polar angles $\theta_{\text{cm}} = 90^\circ \pm 10^\circ$ are found to exhibit isotopic equilibrium. The temperature $T = 6.8$ MeV and the chemical potential for neutrons $\mu_n = -10.2$ MeV derived in grand-canonical approximation suggest a chemical freeze-out at low-density which does not contradict fragments being dynamically pre-formed at higher densities as suggested

in Refs. [13, 32, 33, 45] for similar reactions.

Similar results are also observed at forward angles $\theta_{\text{cm}} \leq 34^\circ$, however with the difference that the measured isotope yield ratios indicate a dominance of projectile matter. The deduced isotopic transparency τ is found to increase from below $\tau \approx 30\%$ for $Z = 1, 2$ particles to a significant value exceeding $\tau \approx 70\%$ for $Z = 4$ isotopes, the heaviest products included in this study. The ${}^4\text{He}$ production deviates from the systematic trend, and possible explanations for the observed anomalously high transparency were presented. The isotopic transparencies are found to be compatible with the isotropy ratios deduced from measured transverse and longitudinal momentum variances and, very generally, show that excess momenta in longitudinal direction are caused by the incomplete stopping of the projectile, even in the selected highly central collisions at this energy.

Acknowledgments

The authors would like to thank the staff of the GSI for providing high-quality ${}^{124,129}\text{Xe}$ beams adapted to the requirements of the INDRA multidetector. Helpful discussions with A.S. Botvina, P. Napolitani and S. Typel are gratefully acknowledged. This work was supported by the European Community under contract No. ERBFMGECT950083 and by the French-German Collaboration Agreement 03-45 between IN2P3 - DSM/CEA and GSI.

References

- [1] Bao-An Li, Che Ming Ko, W. Bauer, *Int. J. Mod. Phys. E* **07** (1998) 147.
- [2] J. Wilczyński, *Nucl. Phys. A* **216** (1973) 386.
- [3] V.V. Volkov, *Phys. Rep.* **44** (1978) 93.
- [4] D.H.E. Gross, H. Kalinowski, *Phys. Rep.* **45** (1978) 175.
- [5] K. Siwek-Wilczyńska, J. Wilczyński, *Nucl. Phys. A* **264** (1976) 115.
- [6] W. Trautmann, U. Milkau, U. Lynen, J. Pochodzalla, *Z. Phys. A* **344** (1993) 447.
- [7] Bao-An Li, *Phys. Rev. Lett.* **88** (2002) 192701.
- [8] P. Danielewicz, R. Lacey, W.G. Lynch, *Science* **298** (2002) 1592.
- [9] A. Le Fèvre, Y. Leifels, W. Reisdorf, J. Aichelin, Ch. Hartnack, *Nucl. Phys. A* **945**, 112 (2016).
- [10] S. Huth, et al., *Nature* **606** (2022) 276.
- [11] W. Reisdorf, et al., *Phys. Rev. Lett.* **92** (2004) 232301.
- [12] A. Andronic, J. Łukasik, W. Reisdorf, W. Trautmann, *Eur. Phys. J. A* **30** (2006) 31.
- [13] K. Zbiri, et al., *Phys. Rev. C* **75** (2007) 034612.
- [14] G. Lehaut, et al., *Phys. Rev. Lett.* **104** (2010) 232701.
- [15] J. Pouthas, et al., *Nucl. Instrum. Methods Phys. Res. A* **357** (1995) 418.
- [16] F. Rami, et al., *Phys. Rev. Lett.* **84** (2000) 1120.
- [17] A. Le Fèvre, et al., *Nucl. Phys. A* **735** (2004) 219.
- [18] A. Le Fèvre, et al., *Phys. Lett. B* **659** (2008) 807.
- [19] F. Lavaud, Ph.D. thesis, Université Louis Pasteur Strasbourg I, Report IPNO-T.01-06 (2001).

- [20] B. Bouriquet, et al., in *Proceedings of the XXXIXth International Winter Meeting on Nuclear Physics, Bormio, Italy*, edited by I. Iori, A. Moroni (Ricerca Scientifica ed Educazione Permanente Suppl. vol. **117**, Milano, 2001), p. 84.
- [21] Bao-An Li, S.J. Yennello, Phys. Rev. C **52** (1995) R1746.
- [22] H. Johnston, et al., Phys. Lett. B **371** (1996) 186.
- [23] R. Ogul, et al., Phys. Rev. C **107** (2023) 054606.
- [24] R. Wada, et al., Phys. Rev. Lett. **58** (1987) 1829.
- [25] J. Pochodzalla, W. Trautmann, in *Isospin Physics in Heavy-Ion Collisions at Intermediate Energies*, edited by Bao-An Li, W.U. Schröder (Nova Science Publ. Inc., New York 2001), p. 451.
- [26] H.W. Barz, H. Schulz, J.P. Bondorf, J. Lopez, K. Sneppen, Phys. Lett. B **211** (1988) 10.
- [27] A.Z. Mekjian, Phys. Rev. C **17** (1978) 1051.
- [28] S. Albergo, S. Costa, E. Costanzo, A. Rubbino, Il Nuovo Cimento **89 A** (1985) 1.
- [29] G.J. Kunde, et al., Phys. Lett. B **416** (1998) 56.
- [30] W. Trautmann, et al., Phys. Rev. C **76** (2007) 064606.
- [31] E. Bonnet, et al., arXiv:2503.23809 [nucl-th] (2025).
- [32] A. Le Fèvre, et al., Phys. Rev. C **100** (2019) 034904 .
- [33] A. Ono, Prog. Part. Nucl. Phys. **105** (2019) 139.
- [34] I. Tanihata, et al., Phys. Lett. **160B** (1985) 380.
- [35] F. Deák, A. Kiss, Z. Seres, A. Galonsky, L. Heilbronn, Phys. Rev. C **43** (1991) 2432.
- [36] H.S. Xu et al., Phys. Rev. Lett. **85** (2000) 716.
- [37] D. Hahn, H. Stöcker, Nucl. Phys. A **476** (1988) 718.
- [38] J.P. Bondorf, A.S. Botvina, A.S. Iljinov, I.N. Mishustin, K. Sneppen, Phys. Rep. **257** (1995) 133.
- [39] A.S. Botvina, O.V. Lozhkin, W. Trautmann, Phys. Rev. C **65** (2002) 044610.
- [40] H.A. Gustafsson, et al., Phys. Rev. Lett. **53** (1984) 544.
- [41] S. Fritz, et al., Phys. Lett. B **461** (1999) 315.
- [42] G. Verde, A. Chbihi, R. Ghetti, J. Helgesson, Eur. Phys. J. A **30** (2006) 81.
- [43] A.S. Botvina, et al., Nucl. Phys. A **584** (1995) 737.
- [44] A.H. Raduta, M. Colonna, M. Di Toro, Phys. Rev. C **76** (2007) 024602.
- [45] T. Génard, Ph.D. thesis, Normandie Université, 2023; NNT: 2023NORMC269, <https://theses.hal.science/tel-04483956>.
- [46] J. Gosset et al., Phys. Rev. C **16** (1977) 629.
- [47] P. Pawłowski, et al., Phys. Rev. C **108** (2023) 044610.
- [48] S. Typel, Phys. Rev. C **89** (2014) 064321.
- [49] J. Tanaka, et al., Science **371** (2021) 260.